Additive Manufacturing xxx (xxxx) xxx

Contents lists available at ScienceDirect

Additive Manufacturing

journal homepage: www.elsevier.com/locate/addma

A new strategy for strengthening additively manufactured cold spray deposits through in-process densification

Ningsong Fan [a], Jan Cizek [b], Chunjie Huang [c], Xinliang Xie [d], Zdenek Chlup [e], Richard Jenkins [a], Rocco Lupoi [a], Shuo Yin [a,*]

[a] Department of Mechanical and Manufacturing Engineering, Parsons Building, Trinity College Dublin, The University of Dublin, Dublin 2, Ireland
[b] Institute of Plasma Physics, The Czech Academy of Sciences, Za Slovankou 1782/3, 182 00 Prague, Czech Republic
[c] Department of Mechanical Engineering, Helmut-Schmidt-Universität/Universität der Bundeswehr, 22043 Hamburg, Germany
[d] Institute of Mechanics, Materials and Civil Engineering, UC Louvain, Louvain-la-Neuve, Belgium
[e] Institute of Physics of Materials, Czech Academy of Sciences, Žižkova 513/22, 616 62 Brno, Czech Republic

ARTICLE INFO

Keywords:
Kinetic spray
Additive manufacturing
Deposition Efficiency (DE)
Heat treatment
Microstructure

ABSTRACT

In this study, a novel strategy for strengthening additively manufactured cold spray deposits is proposed, based on a rather under-explored niche of the processing parameters space. We have shown that a combination of two factors (a wide particle size distribution of the feedstock powder and low processing parameters) triggered a successful implementation of this strategy. At such conditions, a significant proportion of the particles (particularly those with a large size) fail to deposit and rebound after their impact instead, initiating the in-process densification effect: by accepting a small price increase trade-off (the wide range powders are inexpensive), the rebounds result in a severe accumulative plastic deformation of the deposited particles and further reduction in porosity. These, in turn, lead to mechanical properties comparable to those produced under high processing parameters (i.e., using N_2 gas at high temperatures or using expensive and unsustainable He as the propulsive gas). As a welcome benefit, the detrimental thermal effects encountered in cold spraying using high-temperature processing gas (such as oxidation, nitridation and phase changes) can be effectively minimized using the new low parameters strategy. Overall, the aim of this study is to propose a new manufacturing strategy to fabricate high-performance cold sprayed deposits without the use of expensive and unsustainable He gas.

1. Introduction

Cold spray additive manufacturing (CSAM) is a rapid solid-state deposition process which can be utilized to manufacture freestanding parts, fabricate thick coatings on substrates or repair damaged components [1–5]. This technique has been applied for the deposition of various metallic materials including pure metals [6], conventional alloys [7], high entropy alloys [8], amorphous alloys [9] and metal matrix composites [10,11]. In the process, metal feedstock particles are accelerated by compressed gas (typically N_2, He, or their mixture [12]) and propelled toward a target substrate. Upon impact, the particles experience severe plastic deformation and strongly bond with the substrate or previously deposited particles to form a bulk deposit. Importantly, the CSAM technology operates below the melting point of the materials, which makes it unique as compared to fusion-based additive manufacturing methods. The particle impact velocity is the key factor in the process as the particles will likely rebound from the substrate if they fail to reach a critical velocity. The critical velocity is known to mainly depend on the intrinsic properties of feedstock powders (i.e., material properties, morphology and size) and also particle temperature upon impact with the substrate [13–15]. Owing to the variability of the CSAM process, a wide range of particle impact velocities can be attained by selecting different combinations of gas type, gas pressure and temperature.

A number of experimental studies have been conducted to investigate the effect of the particle impact velocity on the microstructure and mechanical properties of the cold sprayed deposits. Even though a wide range of materials and processing parameters were applied, a common conclusion has been drawn in most of these works: a higher particle impact velocity generally leads to denser deposits and better mechanical properties as a result of the enhanced particle plastic deformation [16–20]. Contrary to this general understanding, our previous work

* Corresponding author.
E-mail address: yins@tcd.ie (S. Yin).

https://doi.org/10.1016/j.addma.2020.101626
Received 15 June 2020; Received in revised form 22 August 2020; Accepted 22 September 2020
Available online 29 September 2020
2214-8604/© 2020 The Authors. Published by Elsevier B.V. This is an open access article under the CC BY license (http://creativecommons.org/licenses/by/4.0/).

related to cold sprayed Al deposits [21] showed that this dependence was not described completely; we found a niche at low in-flight impact velocities of the Al particles where the particle plastic deformation and deposit density in fact increased with decreasing velocity. The reason for this somewhat unexpected phenomenon is believed to be the in-process densification effect triggered by a large number of rebound particles hitting the deposit under low impact velocities. In a separate study with regard to cold sprayed Ni coating onto Al substrate, we also identified a similar phenomenon that lower particle in-flight impact velocities actually led to more severe plastic deformation at the coating-substrate interfaces due to rebound particles [22]. As much as the work [21] has confirmed that cold sprayed Al deposits can be densified through the self-peening in-process densification effect, it did not provide an in-depth analysis of the mechanisms triggering the densification, nor did it investigate its impact on mechanical properties, a rather key concern for cold sprayed deposits.

Cold sprayed deposits may exhibit partially deteriorated mechanical properties in the as-fabricated state due to the existence of incomplete interparticle bonds and porosity. As a material frequently used in aerospace and automotive sectors and retain the link to the previous research, cold sprayed Al deposits were selected as the demonstrator. To widen our understanding, heat treatment, a common way to improve the mechanical properties of cold sprayed deposit [23–26], was further applied to the as-fabricated samples, and the obtained results provided an important comparison. The results presented in this study clearly demonstrate that the low processing parameters are capable to provide mechanical properties comparable to the high parameters. Taking advantage of this, we may be able to use economical and sustainable N_2 to replace He for achieving high-performance cold spray parts, while also effectively avoiding the problems encountered in high-temperature cold spray deposition (e.g., oxidation, nitridation, or phase changes of the powder materials). This new manufacturing strategy may direct the further evaluation direction of cold spray technology.

2. Experimental methodology

2.1. Deposit fabrication

Spherical Al powders with a minimum purity of 99.7% (H-30, Valimet Inc., California) were used as the cold spray feedstock. The impurities in the powder mainly include volatile (< 0.1 wt%), grease (< 0.2 wt%) and iron (< 0.2 wt%). The powder diameter range was measured between 10 and 160 μm. Before spraying, the powders were stored under air environment without any pre-processing. Fig. 1 shows the surface morphology of the Al powders observed by SEM (Carl Zeiss ULTRA Plus, Germany) and the corresponding particle size distribution measured by laser scattering particle size distribution analyzer (Horiba LA920, Japan). The Al deposits were then manufactured using an in-house assembled cold spray system (Trinity College Dublin, Ireland, [27]) on thin 6068 Al alloy substrates. The system consists of high-pressure gas from cylinders, gas heater, powder feeder, CNC working platform for controlling the substrate movement, Laval nozzle and computer control system. The nozzle used in this work has a round cross-sectional shape with a convergent length of 30 mm and a divergent length of 180 mm. The inlet, throat and outlet diameters are 10 mm, 2 mm and 6 mm, respectively. Powders were injected exactly at the nozzle inlet plane. The gas temperature and pressure are measured near the nozzle inlet. A self-made custom nozzle cooling jacket was applied to prevent the clogging of nozzle at high temperature. Our previous study has demonstrated that, with increasing particle impact velocity, the density of Al deposits initially decreases to a minimum value, followed by the expected increase trend [21]. Based on that study, three processing parameters combinations (denoted as D1-D3, Table 1 [28]) were selected for the deposition, leading to three different particle in-flight velocities: low, medium and high. The deposition efficiency (DE) of the deposits was determined as the ratio of the deposit weight to the weight of the Al powders consumed in the deposition. The produced deposits were subsequently removed from the substrates and cut into dog-bone shaped samples for mechanical testing by electrical discharge machining (EDM). To provide a comparison with the as-fabricated samples, post heat treatment of the samples was further performed in a tube furnace (Clare 4.0, Clasic, Czech Republic) with the aim of altering mechanical properties of the deposits. The heat treatment process was carried out in Ar-7.5%H_2 atmosphere at the temperature of 300 °C and 4 h dwell time, using a heating rate of 6 °C/min and furnace cooling to room temperature.

2.2. Microstructure characterization

The cross-sectional samples used for microstructural analysis were prepared through resin mounting, metallographic abrasive grinding with SiC papers, and mirror-polishing using silica suspensions. To reveal

Table 1
Three sets of CSAM processing parameters used in this work.

Set annotation	D1	D2	D3
Processing gas	N_2	N_2	He
Gas pressure /MPa	3.0	3.0	3.0
Gas temperature/°C	300	650	20
Nozzle traverse speed/mm s^{-1}	50	50	50
Standoff distance/mm	30	30	30
Powder feed rate/g min^{-1}	63	63	63
Relative particle impact velocity	low	medium	high

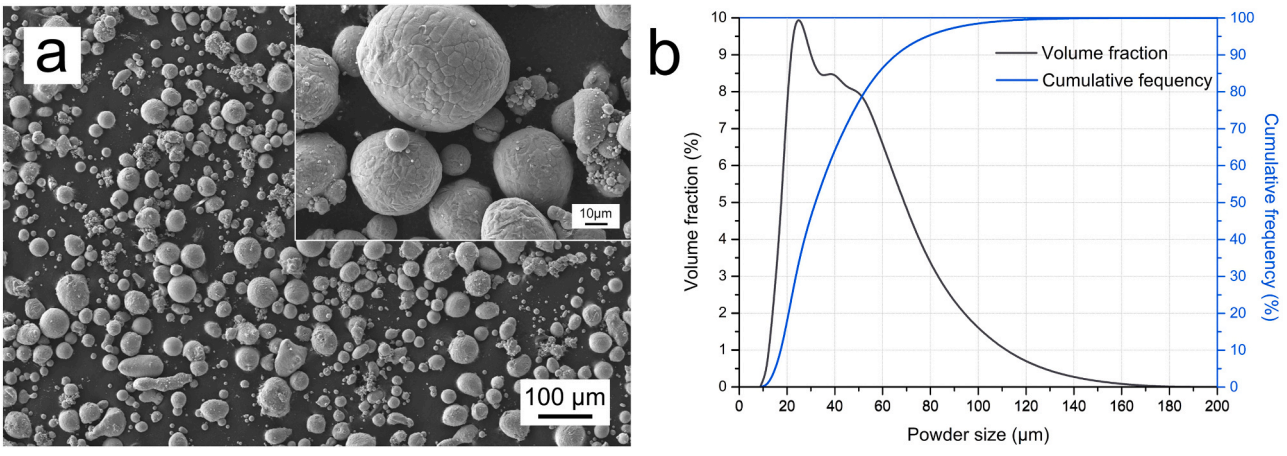


Fig. 1. Al feedstock used in the deposit fabrication: (a) surface morphology, (b) particle size distribution.

the interparticle boundaries and microstructures, the samples were then etched using Keller's reagent (Waterfall & O'Brien Ltd, UK). The cross-sectional morphology of the Al deposits before and after the etching was then characterized by SEM in secondary electron mode. The porosity of the deposits was calculated from light microscope images (Leica DM LM, Germany) using ImageJ analysis software (National Institute of Health, USA). The measurements were averaged from five different deposit areas to ensure the necessary data reliability. To study the plastic deformation behavior of the Al deposits, grain evolution was characterized using electron backscatter diffraction (EBSD). The EBSD data was acquired using a Nordlys EBSD detector with an Aztec control system (Oxford Instruments, UK). Inverse pole figures (IPF) were acquired in order to assess the grain structure within the deposits and to determine the grain size distribution. The grain size analysis was conducted based on an $80 \times 60\ \mu m^2$ EBSD map for each deposit using Chanel 5 post-processing software (Oxford Instruments HKL). A standard noise extrapolation was applied on the maps before the grain analysis. Grains were identified if their grain boundary misorientation was higher than 10°, and the grains at the fringe of the EBSD map were excluded from the data analysis. Electron channeling contrast imaging (ECCI) was also acquired at short SEM work distances for the D1 deposit to complement the EBSD analysis results.

2.3. Mechanical properties measurement

The microhardness of the Al deposits was measured by Vickers hardness indenter (MVK-H1, Mitutoyo, Japan) with an applied load of 100 g for 10 s at room temperature ($HV_{0.1}$). For each sample, 12 indentations were made at randomized positions of the polished cross-sections. In the average value calculation, the obvious outlying values were disregarded. The morphology of the indentions was characterized by light microscopy. To determine the mechanical properties of the cold-sprayed Al deposits, the EDM-machined dog-bone samples with a gauge length of 25 mm, a width of 8 mm and a thickness of 2 mm were measured until a complete fracture of the sample using a universal tensile testing machine (Instron 3366, US) at a cross-head displacement rate of 1 mm/min. Since only ultimate tensile strength (UTS) and elongation at break (EL) were studied in this work, no extensometer was attached and the displacement of the samples was determined by measuring the final gauge length after facture based on the standard ASTM E8 method. The UTS and EL were calculated as average from three (D1, D2) or two (D3) specimens. To analyze the failure mechanisms, the morphology of the fractured surfaces was then observed using SEM.

3. Results and discussion

3.1. Microstructure, density and deposition efficiency

Fig. 2 shows the microstructure of the Al deposits produced under different particle impact velocities in as-fabricated and heat-treated states. In both conditions, the deposits fabricated at the low and high velocities (D1 and D3) exhibited nearly fully dense structure, while that sprayed at the medium velocity (D2) showed a presence of pores and partially visible interparticle boundaries. This result is consistent with our previous study where we found that higher kinetic energy did not always lead to a denser deposit due to the in-process densification effect under low particle impact velocity [21]. The detailed density measured by image analysis is provided in Fig. 3. The relative density of the D1 deposit was 99.93 ± 0.01%, i.e., much higher than that of the D2 deposit (95.76 ± 0.30%) and in fact even slightly higher than that of the D3 deposit (98.47 ± 0.27%). Fig. 3 further shows the deposition efficiency of the three runs; as expected, the high particle velocity resulted in a superior deposition efficiency of almost 65%. Contrary to this, the D1 deposit was formed with an extremely low deposition efficiency, reaching 2% only.

After the heat treatment, the microstructures of the D2 and D3 exhibited a rather notable increase in the density (Figs. 2d–f and 3). Given its original as-fabricated density of 99.93 ± 0.01% triggered by the improved interparticle diffusion and metallurgical bond, the D1 deposit suggested as a slight decrease in fact; this change was, however, within the measurement error range. The measured density provided in Fig. 3 was in good agreement with the microstructure observations, and both density curves (heat-treated and as-fabricated deposits) followed

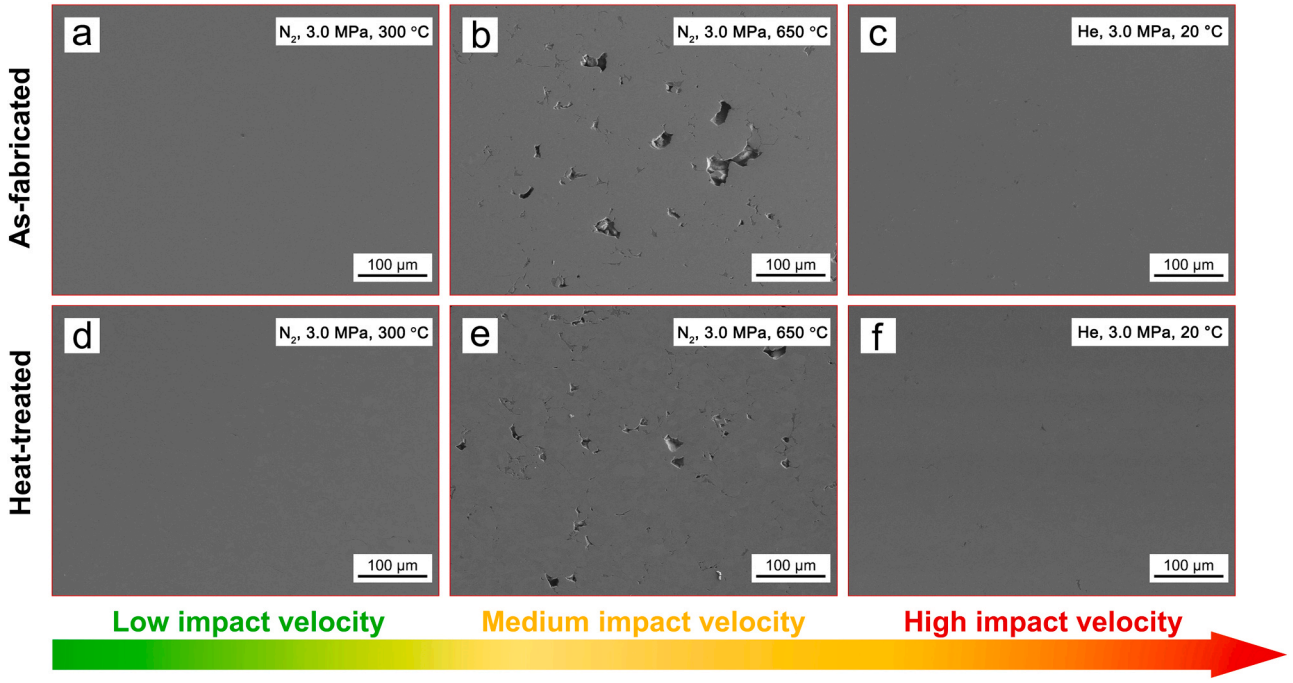


Fig. 2. Microstructure of the cold sprayed Al deposits fabricated under different particle impact velocities in as-fabricated (top row) and heat-treated (bottom row) conditions.

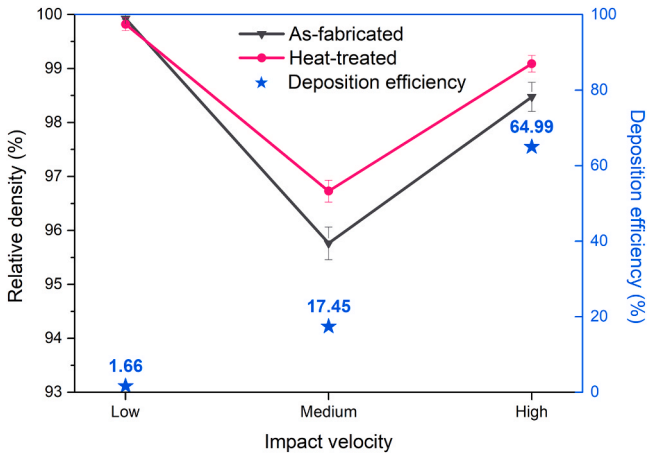


Fig. 3. Density and deposition efficiency of the cold-sprayed Al deposits before and after heat treatment. Note the minimum density values for the medium impact velocity.

the same trend when increasing the particle impact velocity.

To further clarify the particle deposition behavior under the different impact velocities, Fig. 4 shows the etched microstructures and the corresponding binary images of the Al deposits with different particle impact velocities in the as-fabricated state. After etching, the interparticle boundaries of the deposits were revealed and it was observed that the originally spherical Al powders were flattened to different extents after their deposition. The particles in the D1 deposit underwent a significantly higher extent of plastic deformation than the other two cases (i.e., D2 and D3). The particles were severely deformed into lamellae flattened in the deposition direction. The individual lamellae were not perfect, exhibiting numerous protrusions and asperities, formed by material displacement induced by repetitive impacts of other particles. Their existence triggered a mutual interlocking effect as marked by the yellow arrows which further improved the mechanical properties of the D1 deposit. This is in direct contrast to the D2 deposit where flattening of the deposited particles was much less significant. Furthermore, pores between the particles were clearly visible despite the higher particle impact velocity. As the impact velocity further increased, the extent of the particle deformation in the D3 deposit increased again, bringing along a closure of the pores. This observation suggests that the D1 deposit produced under the low particle impact velocity experienced the most severe plastic deformation, followed by the D3 deposit and finally the D2 deposit.

In cold spray, severe plastic deformation always results in grain refinement due to the occurrence of dynamic recrystallization [29]. Therefore, in order to understand the grain structure of the Al deposits fabricated at different particle impact velocities, Figs. 5 and 6 show the IPF maps and grain size data of the as-fabricated deposits obtained through EBSD. The deformed Al particles in different deposits exhibited a significant difference in grain sizes. Notably, the average and median grain size in the D1 deposit were much smaller than the other two cases, with 53% of the total grains having sub-micron size. This result clearly indicates that the particles in the D1 deposit experienced the most extensive grain refinement due to the rebound particle induced severe plastic deformation. In the D2 deposit, as the number of rebound particles reduced, the plastic deformation of the particles was significantly weaker and therefore the average and median grain size demonstrated an increment from 1.15 μm to 1.43 μm and from 0.96 μm to 1.13 μm, respectively. Also, the frequency of sub-micron-sized grains was reduced from 53% to 39%. For the D3 deposit, a bi-modal grain size structure characterized by a mixture of coarse grains and impact-induced fine grains was observed. This is a typical grain structure that has been frequently seen in cold sprayed deposits produced under high deposition efficiency [30,31]. The bi-modal grain structure typically suggests that the particle central region was less deformed, and this is because of the absence of the rebound-induced repetitive deformation. With the rebound-induced deformation suppressed for the D3 deposit, the grain sizes were still smaller (average of 1.03 μm and median of 1.33 μm) than in the case of the D2 deposit. This is because the severe plastic deformation and grain refinement triggered by the high in-flight velocity (i.e., impact-induced) prevailed and governed the grains formation at the localized interfacial regions. The frequency of sub-micron-sized grains (46%) of the D3 deposit was higher than that of the D2 deposit. The EBSD grain size analysis is consistent with the observations from the

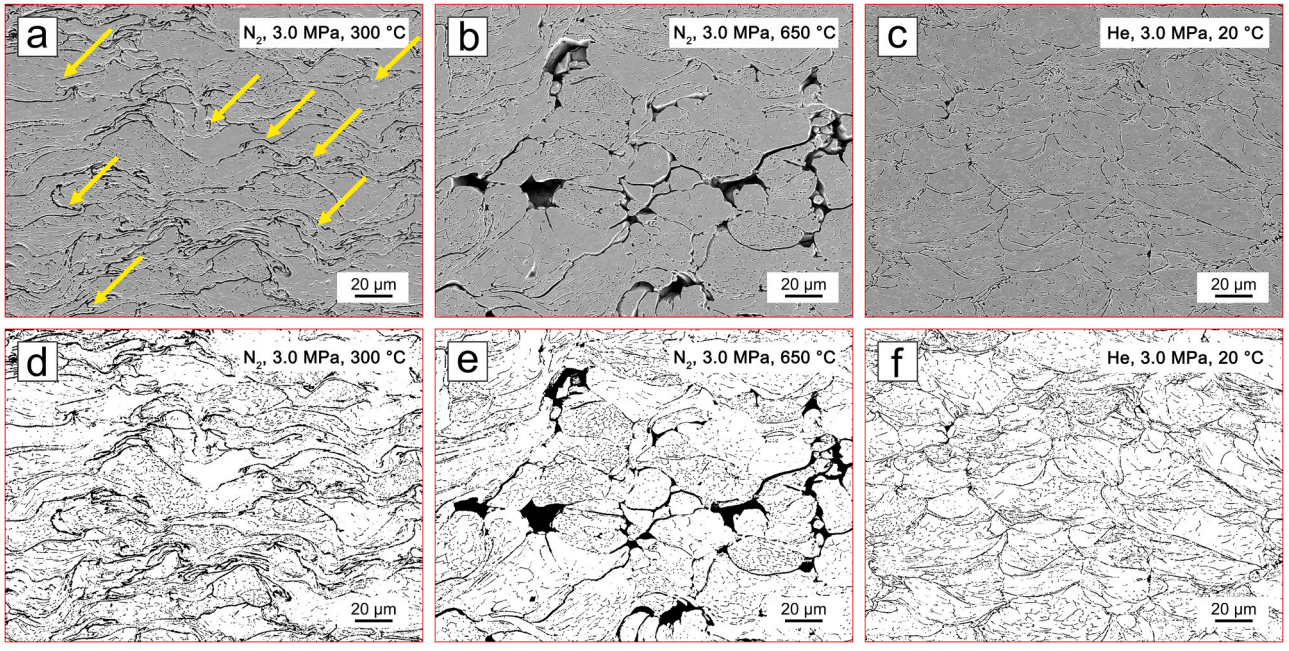


Fig. 4. Etched microstructure (upper row) and the corresponding binary images (lower row) of the as-fabricated Al deposits fabricated under different particle impact velocities: (left) D1, (middle) D2, (right) D3. The interlocks were marked with yellow arrows. (For interpretation of the references to colour in this figure legend, the reader is referred to the web version of this article.)

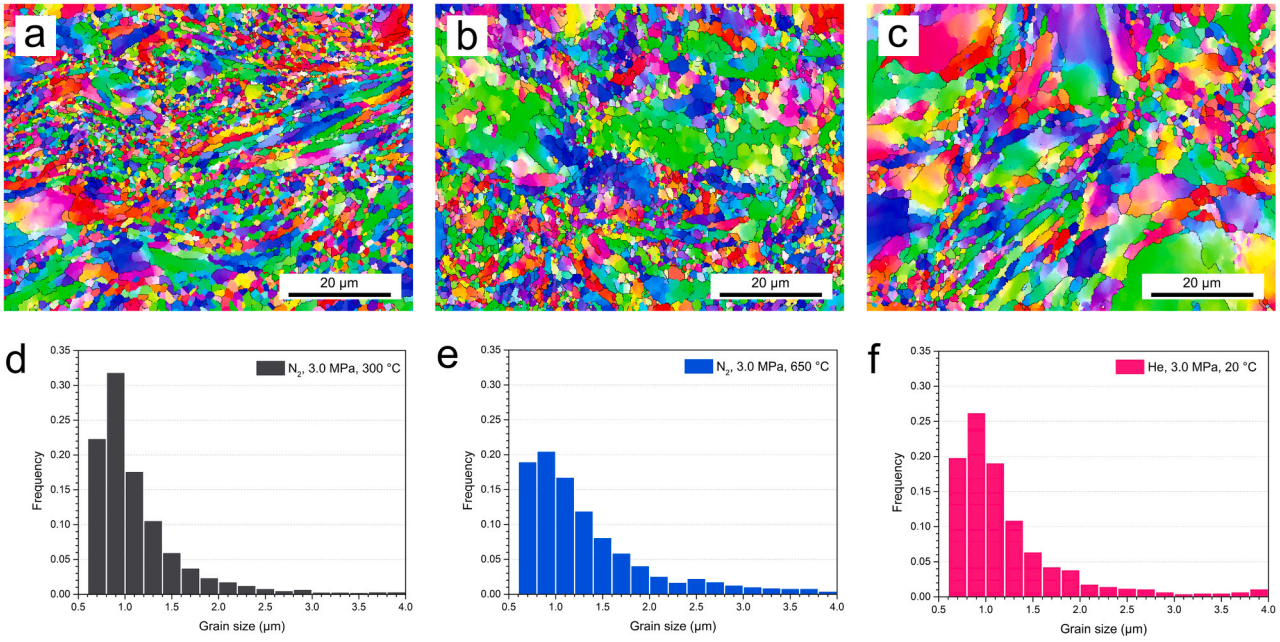


Fig. 5. IPF EBSD maps and grain size distribution of the as-fabricated Al deposits fabricated under different particle impact velocities: (left) D1, (middle) D2, (right) D3.

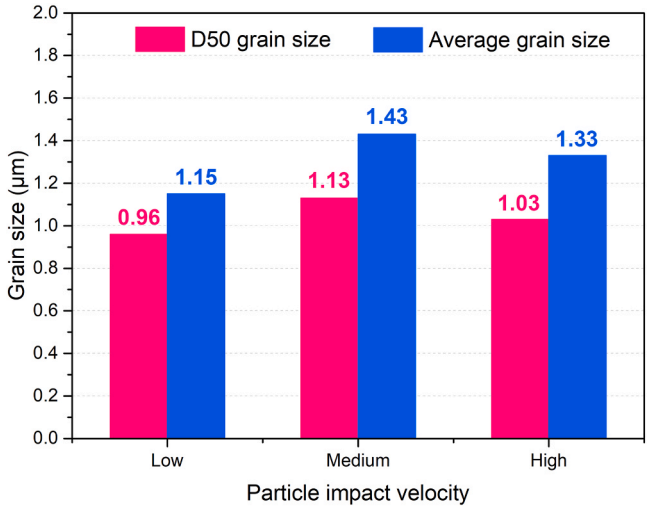


Fig. 6. Average and median (D_{50}) grain size of the cold-sprayed Al deposits in the as-fabricated state.

etched SEM images shown in Fig. 4: the D1 deposit experienced the most extensive plastic deformation, followed by the D3 deposit and then the D2 deposit.

To study the grain refinement behavior in the D1 deposit in more detail, ECCI and a corresponding IPF map were acquired from identical region of the sample (Fig. 7). The interparticle boundaries can be clearly recognized from Fig. 7a, where all the particles were found severely deformed into flattened lamellae shape. From the IPF map shown in Fig. 7b, it can be seen that the grains in most particles were completely refined into equiaxed ultrafine grains due to the severe plastic deformation. Infrequently, a bi-modal grain structure was also identified in few large particles (one such is highlighted by black rectangle in Fig. 7b). The bi-modal grain structure in the D1 deposit could only be seen in the cores of large particles as such central parts of large particles are more difficult to be deformed severely by the repetitive impacts, as opposed to their small counterparts. A close-up view of the black rectangle is shown in Fig. 7c, showing the coarse-fine transition zone and the size differences.

Fig. 8 shows the etched microstructures and the corresponding binarized images of the Al deposits with different particle impact velocities in the heat-treated state. In the heat-treated deposits, the interparticle interfaces of the three deposits became less visible due to the improved interparticle diffusion and metallurgical bond. Aside from this, the same trend was observed as the impact velocity was increased

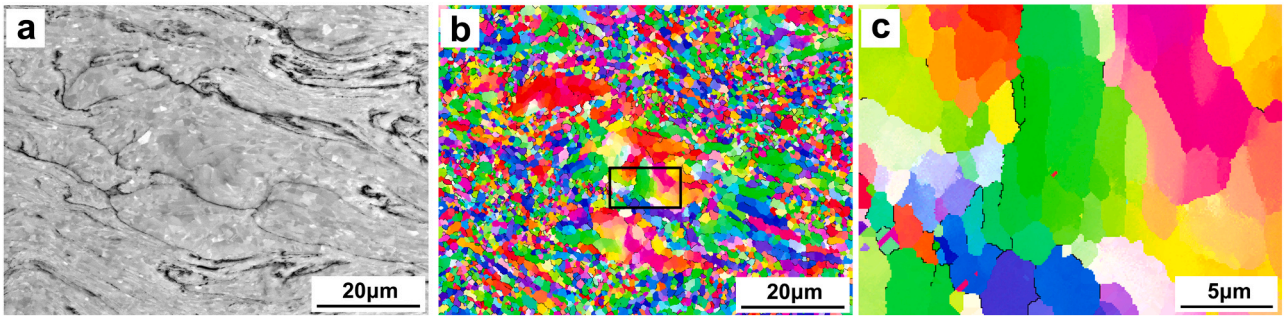


Fig. 7. . ECCI and IPF maps of the as-fabricated D1 Al deposit: (a) ECCI, (b) IPF map and (c) magnified IPF map of the black square in (b).

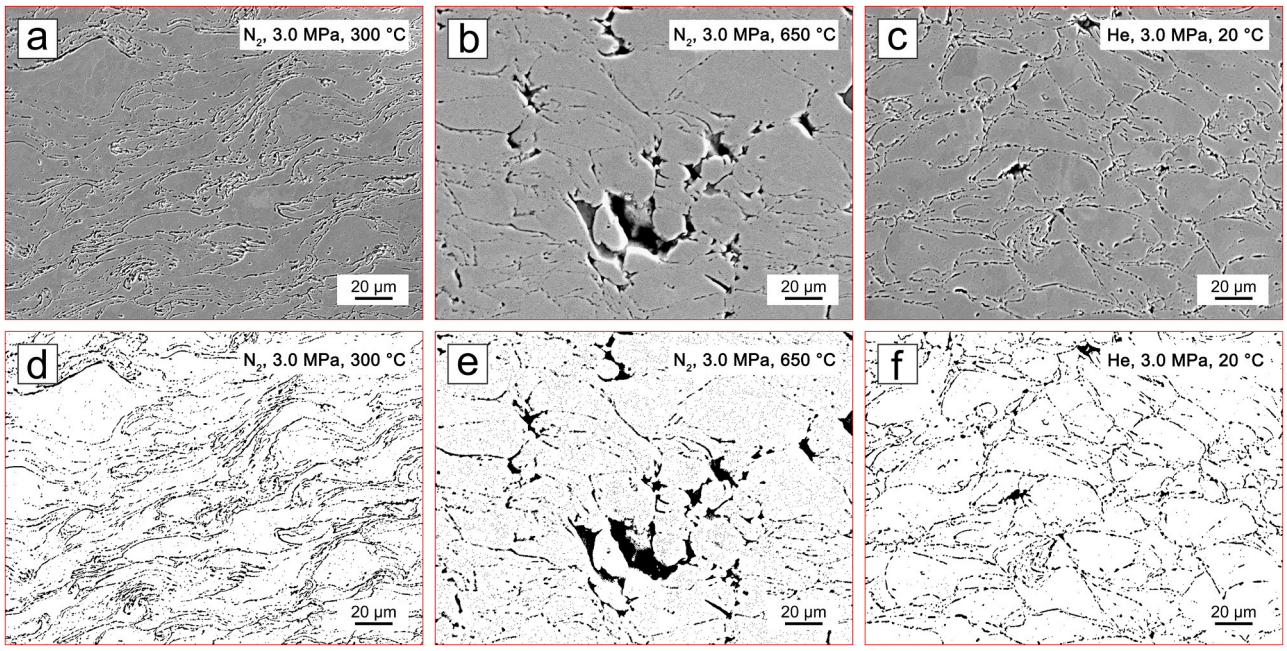


Fig. 8. Etched microstructure (upper row) and the corresponding binary images (lower row) of the heat-treated Al deposits fabricated under different particle impact velocities: (left) D1, (middle) D2, (right) D3.

for the heat treated samples when compared with the as-fabricated state.

3.2. Mechanical properties

Fig. 9 shows the $HV_{0.1}$ microhardness results of the cold-sprayed Al deposits and the corresponding morphology of the indents in both as-fabricated and heat-treated states. It is evident that in the as-fabricated condition, the D1 deposit exhibited a microhardness very similar to the D3 deposit, with both being higher than that of the D2 deposit (note the error values). This is due to the increased plastic deformation and work hardening experienced by the D1 and D3 deposits [21]. As expected, the microhardness of all deposits reduced significantly after the heat treatment due to the suppression of the work hardening effect [23,32]. In addition, all indents maintained a diamond shape with no obvious micro-cracks formed near their corners, indicating the good toughness of the cold sprayed Al deposits. Also, in the as-fabricated state, deformation pile-up of the material in the vicinity of the indent was observed for all three samples. This is not visible after the heat-treatment, which could probably be attributed to improved plasticity.

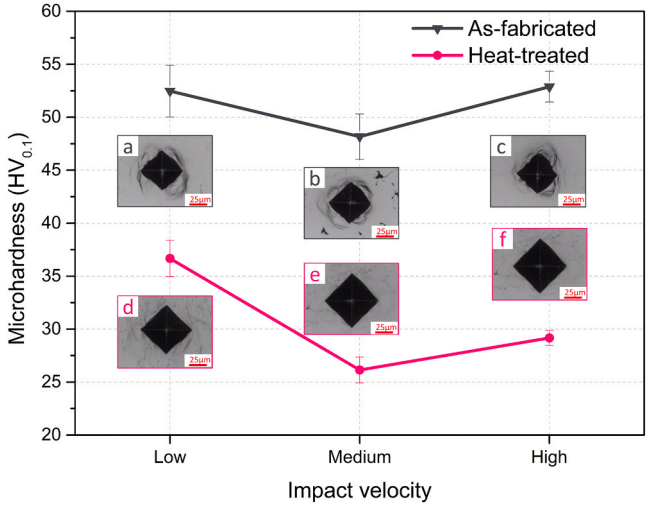


Fig. 9. $HV_{0.1}$ microhardness of the cold-sprayed Al deposits and the corresponding morphology of indents in the as-fabricated and heat-treated conditions.

Fig. 10 shows the UTS and EL of the cold-sprayed Al deposits in the as-fabricated and the heat-treated states obtained from the uniaxial tensile testing. As can be seen from Fig. 10a, all the as-fabricated Al deposits exhibited a limited ductility due to the nature of cold spray [20]. By comparing the three deposits, it can be seen that the D2 deposit exhibited lower UTS and EL than the D1 and D3 deposits owing to the porous structure and inferior interparticle bond. Importantly, the D1 deposit was about 12% stronger than the D3 deposit while having a similar ductility. After the heat treatment, the EL of all deposits significantly improved to 17.91%, 6.88% and 17.84% for the D1, D2 and D3, respectively, as shown in Fig. 10b due to the enhanced interparticle bond and reduced work hardening [33]. In contrast, the UTS decreased sharply by 57–66% because of annealing.

Fig. 11 shows the fracture surfaces of the cold-sprayed Al deposits in the as-fabricated condition. As shown in Figs. 11a and d, in the D1 deposit, the layer-by-layer structure in the direction of deposition was clearly discernible and the fracture dominantly propagated along the interfaces of interparticle (inter-particle decohesion). Limited dimple-like features can be recognized on the fracture surface as indicated by the yellow arrow. For the D2 deposit, the fracture mechanism remained the same as for the D1 deposit, but the less flattened particles resulted in a significantly smoother fracture surface where no dimple-like features were observed. The fractographic character is in line with the mechanical test results where the D2 deposit had the lowest ductility due to the poor interparticle bond as a result of insufficient plastic deformation. The fractographic images of the D3 deposit shown in Figs. 11c and f also demonstrated limited dimple-like features as marked by the yellow arrow, indicating an improved ductility of the D3 deposit than the D2 deposit. Overall, all the deposits showed a prevalently brittle fracture. In addition, the fractographic images also demonstrated that the particles in the D1 deposit experienced the most severe plastic deformation, which is in accordance with the cross-sectional microstructure analysis shown in Fig. 4.

Fig. 12 shows the fracture surfaces of the heat-treated deposits. As expected, the heat treatment triggered a partial recovery of plasticity,

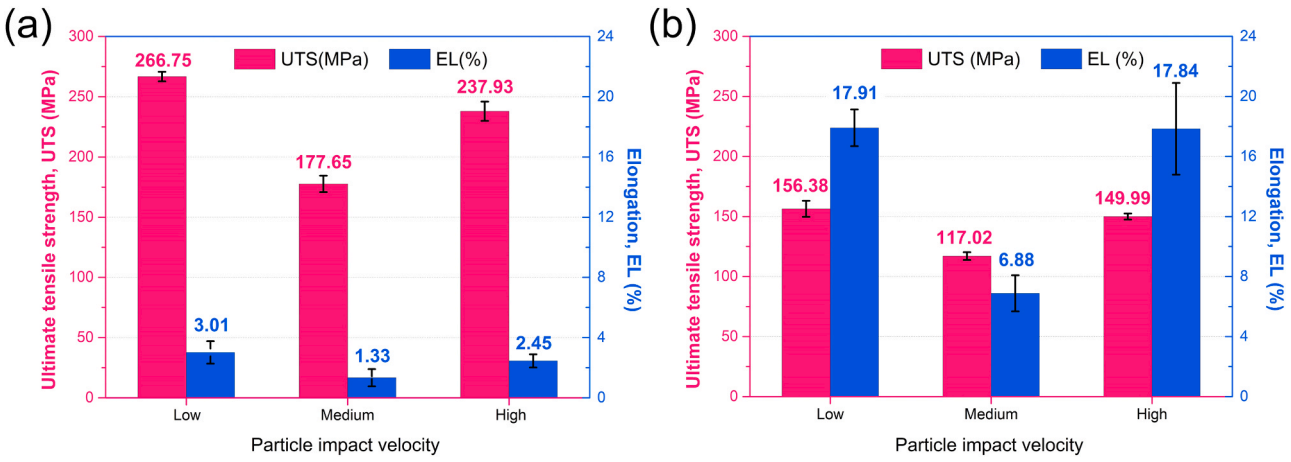


Fig. 10. The ultimate tensile strength (UTS) and elongation (EL) of cold-sprayed Al deposits fabricated with different particle impact velocities in the (a) as-fabricated; (b) heat-treated conditions.

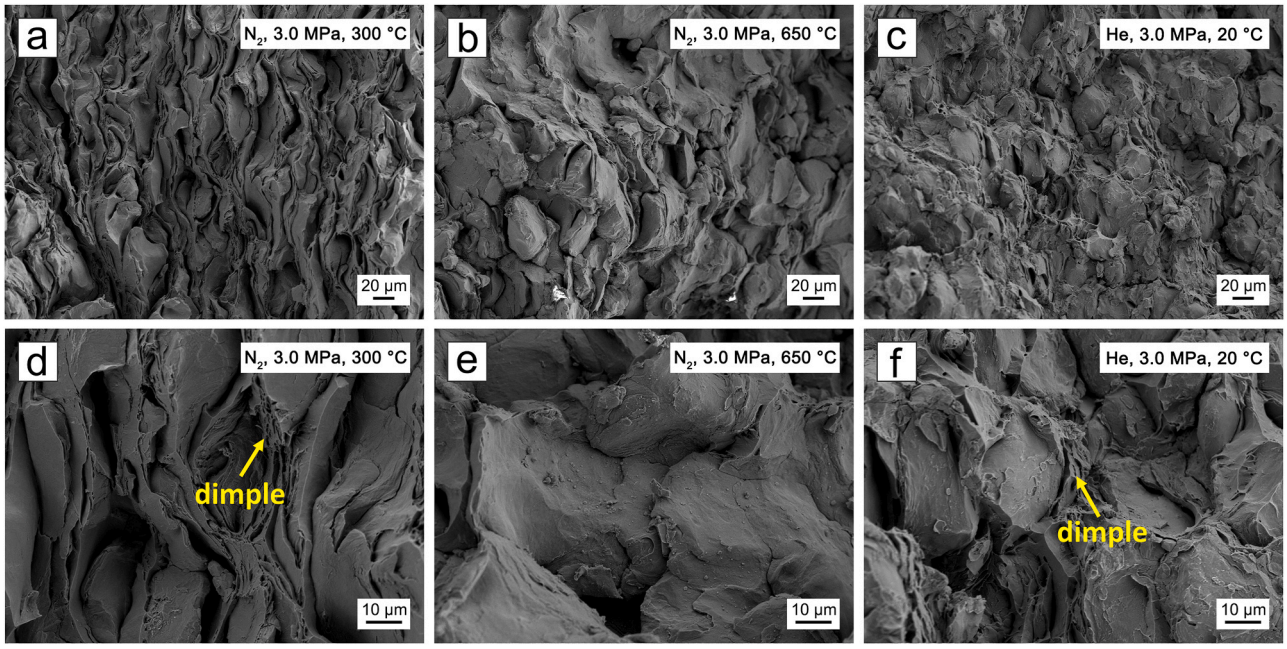


Fig. 11. Fractographic analysis of the fracture surface of cold-sprayed Al deposits in the as-fabricated condition (a, d) D1, (b, e) D2, and (c, f) D3. (For interpretation of the references to colour in this figure legend, the reader is referred to the web version of this article.)

manifested by a larger number of dimple-like features, indicating ductile fracture mode, observed on the fracture surfaces of all deposits. Partial trans-particle crack propagation was observed in all three cases, indicating an improved interparticle bond than in the as-fabricated state. The increase in the dimple-like features quantity of the D1 deposit was not so pronounced as opposed to the other two cases. It is therefore surprising that its ductility was markedly better than the D2 deposit (Fig. 10b); in fact, it was comparable to the D3 deposit. A potential explanation is due to the interlocking phenomenon of the particles in the D1 deposit. By mutually comparing the D2 and D3 deposits, it is seen that the dimples at the fracture surface of the D3 deposit were actually larger than those for the D2 deposit, suggesting a better plasticity recovery, in line with the ductility results.

3.3. Strengthening mechanisms

In cold spray, a general understanding of the relationship between the particle impact velocity and density or mechanical properties is that a higher velocity leads to denser deposits and superior mechanical properties. Contrary to this, in this work, an interesting phenomenon was investigated in more detail: at low impact velocity, the Al deposit can deliver improved density and mechanical properties comparable to that produced under high impact velocity, while the deposit fabricated under medium impact velocity possessed the lowest density and the worst mechanical properties of the three.

When the particle impact velocity exceeds a critical velocity, a cold sprayed deposit can be formed. Both the impact velocity and the critical velocity are size-dependent parameters: generally, as the particle size increases, the critical velocity reduces, while the particle impact velocity increases first and then turns to a decrease [21]. As a result, for given processing conditions, there is always a velocity range (so called deposition window, which is a function of the particle size), within which a successful deposition can be expected [34,35]. Fig. 13 plots the deposition window of the Al powder, assuming the processing conditions used in this work. The critical velocity was calculated using KSS software (Kinetic Spray Solutions, Germany), while the actual particle impact

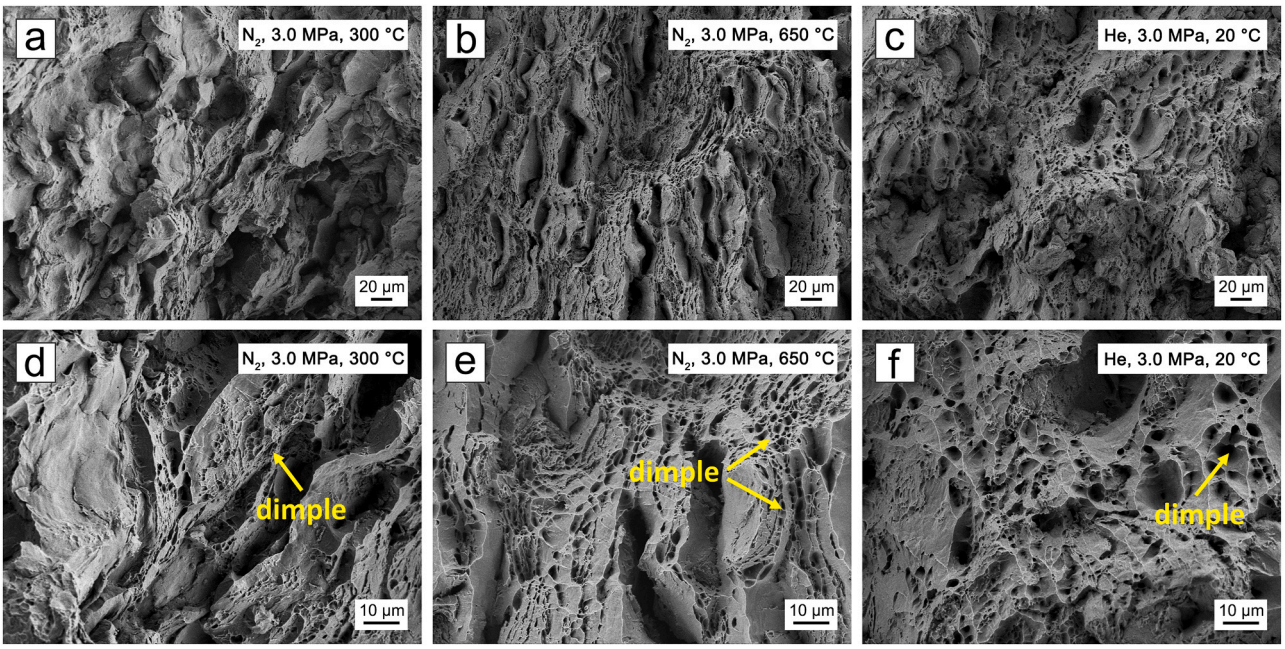


Fig. 12. Fractographic analysis of the fracture surface of cold-sprayed Al deposits in the heat-treated condition. (a, d) D1, (b, e) D2, and (c, f) D3.

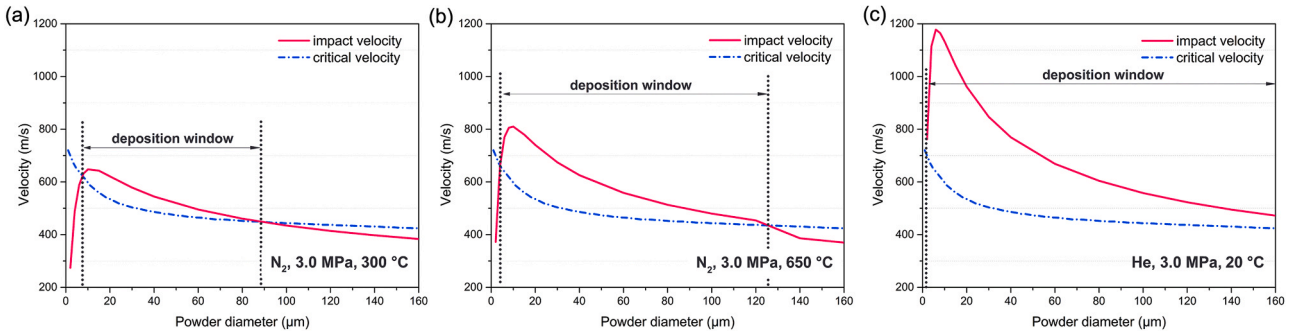


Fig. 13. Calculated impact and critical velocities of Al powder particles as a function of their diameters. The particles would deposit as long as their velocity is higher than the critical value. Note the significant difference in the sprayable ranges among the three different processing parameter sets used in this work: (a) D1, (b) D2, and (c) D3.

velocity was calculated using Ansys-Fluent. Both methods have been widely used in the field of cold spray for predicting particle impact velocity and critical velocity [36,37]. The powder feedstock used in this work had a wide particle size distribution, from 10 μm up to 160 μm (Fig. 1). It is worth noting that the estimation of the particle critical velocity plotted in Fig. 13 did not consider particle temperature. Actually, higher particle temperature will lead to reduced critical velocity [34], but it is difficult to quantify the influence of particle temperature on critical velocity. Therefore, in this work, we assumed that the critical velocities of Al particles were same for the three tests. Under the low impact velocity conditions (N_2, 3.0 MPa, 300 °C), the deposition window and thus the powder size range for a successful deposition were rather narrow, as schematized in Fig. 13a. Naturally, a significant proportion of the particles were outside the deposition window, particularly those with the large size. As a consequence, the big particles rebounded from the substrate after impacting, instead of being deposited. This fact

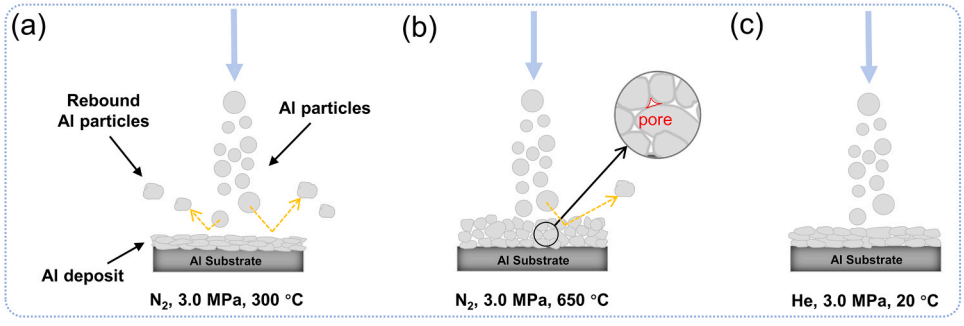


Fig. 14. Schematic illustration of different strengthening mechanisms occurring at different spray conditions encountered while cold spraying Al deposits. At low velocity conditions (D1, left), the big particles were outside the deposition window and therefore could not deposit. Their impacts densified the deposit and triggered an extensive plastic deformation. At medium conditions (D2, middle), the effect was much less exhibited, leaving some non-closed pores in the deposit. At high velocities (D3, right), all particles deposited, resulting in a very high deposition efficiency.

is reflected in the low deposition efficiency of D1, shown in Fig. 3. Through their impacts, the rebound particles continuously compacted the already formed deposit and densified it by inducing further plastic deformation, as schematized in Fig. 14a. In order to further confirm the role of these large particles, a comparison experiment was conducted using different Al powders (Toyal Europe, France) with a size range of 20–50 μm (i.e., large powders were removed). The resultant deposit was less dense than the one produced using large size-range powders (10–160 μm), which confirms the critical role of large particles. A detailed description of the comparison experiment and result analysis are provided in the Supplementary material. By this in-process densification mechanism, the interparticle metallurgical bond can be enhanced [38]. In addition, the in-process densification also caused significant interlocking in the deposit through flattening of the deformed particles, as shown in Fig. 4(a). The interlocking also contributed to the improvement of mechanical properties (high UTS and EL).

When the spray parameters were increased (N_2, 3.0 MPa, 650 °C), the deposition window became wider, enabling more particles deposit successfully (Fig. 13b). The number of rebound particles that were able to densify the deposit was reduced dramatically, resulting in a significant reduction of the total plastic deformation and leading to a relatively high porosity formation and weak interparticle interfaces, as schematized in Fig. 14b. This resulted in the lowest UTS and EL values of the D2 deposit. When changing the gas from N_2 to He (He, 3.0 MPa, 20 °C), the in-flight velocities were the highest and therefore the particle size range for a successful deposition became the largest, as shown in Fig. 13c. Theoretically, this means that the number of rebound particles of the used Al powder should be approaching zero. For the real experiment, it is safe to assume that the number of rebound particles was reduced significantly, as reflected in the 65% deposition efficiency shown in Fig. 3. The particles sprayed under this condition experienced much more severe plastic deformation due to their significantly increased kinetic energy (Fig. 14c). While this principle is entirely different from that of the D1 deposit, this mechanism could too result into a major improvement of metallurgical bond between the deposit particles [39]. As a result, the mechanical properties of the D3 deposit were better than those of the D2 deposit, comparable to those of the D1 deposit.

3.4. Advantages of the new strategy

Higher density and imrproved mechanical properties are always desirable for additively manufactured deposits. In cold spray, this can be achieved by increasing either the pressure or the temperature of the processing gas (N_2 in this study). However, the increased gas temperature may lead to increased oxidation, nitridation, phase changes, softening or even melting of particles, as well as damage of the cold spray nozzle made of polymers [40]. Further, the excessive impact velocities at such conditions may trigger corrosion on the substrate surface [34,41]. These problems can, to a certain extent, be avoided with the usage of He as the processing gas. Unfortunately, as opposed to the relatively cheap and sustainable N_2, the high cost of He is economically unfavorable and the reserves of He are limited on Earth. Naturally, the overall trend in cold spray industry is, therefore, to avoid using He. As a third alternative, a targeted adding of peening particles into the feedstock to densify the cold sprayed deposits also improves their mechanical properties; for example, adding large stainless steel particles into Al and its alloys, Ni and Ni-based alloy, Ti and Ti-based alloy powders [42–47], adding Al_2O_3 particles into A380 alloy powders [48] or adding Cu_2O particles into Cu powders [49]. There are different names for this kind of strengthening processes, such as “in-situ shot peening” [44,45,50], “in-situ forging” [42,43,46], “self-peening” [51,52]. However, one thing in common for these processes is that the peening effect was achieved through the impact and rebound of foreign powders that are different from cold sprayed powders. These foreign particles are likely to partially embed and result in unwanted stress concentrations, pores formation, and localized chemical heterogeneities. The additional powder mixing procedure also increases workload and manufacturing cost. The presented study suggests yet another alternative: using powder feedstock with wide size range distribution and low gas processing parameters to produce dense cold sprayed deposits with high mechanical properties. With this method, we do not need to introduce foreign powders and additional powder mixing procedure; the peening is completely achieved through the impact and rebound of the coarse powders in the feedstock. Note that powders with wide size range are typically inexpensive, significantly cheaper than those with narrow size ranges. At the expense of slightly increased costs of powders due to low deposition efficiency, this novel strategy can avoid all the aforementioned problems brought by foreign peening particles and presents an interesting alternative to spraying either at high temperatures or using expensive and unsustainable He.

4. Conclusions

A novel strategy for the fabrication of high-performance cold sprayed Al deposits is presented in this paper. Instead of using high processing parameters that are either uneconomical (when using helium as the propulsion gas) or may lead to detrimental effects such as increased oxidation, nitridation, phase changes, corrosion of the substrate or even damage to the expensive spray nozzle (when using gases at high temperatures), the proposed procedure is based on a mutual incidence of two factors: a wide particle size distribution of the feedstock powder, and very low processing parameters (N_2 propulsion gas at low temperature). The synergistic effect of the two factors not only effectively eliminates the said detrimental effects, but also triggers an in-situ densification of the deposits. Remarkably, this results in a significant improvement of the microstructure and the associated mechanical properties, reaching or even surpassing those of the deposits formed at the high process parameters (e.g., the tensile strength value improvement by 12%). Performing a heat treatment induces a trade-off between a reduced strength of all samples and their improved ductility, but the deposits prepared under low parameters still retain their superior properties. In general, this new manufacturing strategy may open a new direction for cold spray research of high-performance structural materials.

CRediT authorship contribution statement

Ningsong Fan: Writing - original draft, Investigation, Formal analysis. **Jan Cizek**: Methodology, Investigation. **Chunjie Huang**: Resources. **Xinliang Xie:** Investigation. **Zdenek Chlup**: Investigation. **Richard Jenkins**: Conceptualization. **Rocco Lupoi**: Project administration. **Shuo Yin**: Supervision, Conceptualization, Methodology, Formal analysis, Writing - review & editing.

Declaration of Competing Interest

The authors declare that they have no known competing financial interests or personal relationships that could have appeared to influence the work reported in this paper.

Acknowledgements

Mr. Ningsong Fan and Dr. Shuo Yin acknowledge the financial support from the China Scholarship Council (No. 201906460020). Dr. Chunjie Huang acknowledges the financial support from the Alexander von Humboldt Foundation. Dr. Rocco Lupoi acknowledges Enterprise Ireland project number IP 2018 0730. The authors also would like to thank the Advanced Microscopy Laboratory (AML) of Trinity College Dublin for the support in data acquisition.

Appendix A. Supporting information

Supplementary data associated with this article can be found in the online version at doi:10.1016/j.addma.2020.101626.

References

[1] S. Yin, P. Cavaliere, B. Aldwell, R. Jenkins, H. Liao, W. Li, R. Lupoi, Cold spray additive manufacturing and repair: fundamentals and applications, Addit. Manuf. 21 (2018) 628–650, https://doi.org/10.1016/j.addma.2018.04.017.
[2] W.Y. Li, K. Yang, S. Yin, X. Yang, Y. Xu, R. Lupoi, Solid-state additive manufacturing and repairing by cold spraying: a review, J. Mater. Sci. Technol. 34 (2018) 440–457, https://doi.org/10.1016/j.jmst.2017.09.015.
[3] X. Wang, F. Feng, M.A. Klecka, M.D. Mordasky, J.K. Garofano, T. El-Wardany, A. Nardi, V.K. Champagne, Characterization and modeling of the bonding process in cold spray additive manufacturing, Addit. Manuf. 8 (2015) 149–162, https://doi.org/10.1016/j.addma.2015.03.006.
[4] R.N. Raoelison, Y. Xie, T. Sapanathan, M.P. Planche, R. Kromer, S. Costil, C. Langlade, Cold gas dynamic spray technology: a comprehensive review of processing conditions for various technological developments till to date, Addit. Manuf. 19 (2018) 134–159, https://doi.org/10.1016/j.addma.2017.07.001.
[5] W. Li, C. Cao, S. Yin, Solid-state cold spraying of Ti and its alloys: a literature review, Prog. Mater. Sci. 110 (2019), 100633, https://doi.org/10.1016/j.pmatsci.2019.100633.
[6] T. Suhonen, T. Varis, S. Dosta, M. Torrell, J.M. Guilemany, Residual stress development in cold sprayed Al, Cu and Ti coatings, Acta Mater. 61 (2013) 6329–6337, https://doi.org/10.1016/j.actamat.2013.06.033.
[7] S. Bagherifard, A. Heydari Astaraee, M. Locati, A. Nawaz, S. Monti, J. Kondás, R. Singh, M. Guagliano, Design and analysis of additive manufacturedbimodal structures obtained by cold spray deposition, Addit. Manuf. 33 (2020), 101131, https://doi.org/10.1016/j.addma.2020.101131.
[8] S. Yin, W. Li, B. Song, X. Yan, M. Kuang, Y. Xu, K. Wen, R. Lupoi, Deposition of FeCoNiCrMn high entropy alloy (HEA) coating via cold spraying, J. Mater. Sci. Technol. 35 (2019) 1003–1007, https://doi.org/10.1016/j.jmst.2018.12.015.
[9] J. Henao, A. Concustell, I.G. Cano, S. Dosta, N. Cinca, J.M. Guilemany, T. Suhonen, Novel Al-based metallic glass coatings by cold gas spray, Mater. Des. 94 (2016) 253–261, https://doi.org/10.1016/j.matdes.2016.01.040.
[10] S. Yin, J. Cizek, C. Chen, R. Jenkins, G. O'Donnell, R. Lupoi, Metallurgical bonding between metal matrix and core-shelled reinforcements in cold sprayed composite coating, Scr. Mater. 177 (2020) 49–53, https://doi.org/10.1016/j.scriptamat.2019.09.023.
[11] S. Yin, Y. Xie, J. Cizek, E.J. Ekoi, T. Hussain, D.P. Dowling, R. Lupoi, Advanced diamond-reinforced metal matrix composites via cold spray: properties and deposition mechanism, Compos. Part B Eng. 113 (2017) 44–54, https://doi.org/10.1016/j.compositesb.2017.01.009.
[12] W. Wong, E. Irissou, A.N. Ryabinin, J.G. Legoux, S. Yue, Influence of helium and nitrogen gases on the properties of cold gas dynamic sprayed pure titanium coatings, J. Therm. Spray. Technol. 20 (2011) 213–226, https://doi.org/10.1007/s11666-010-9568-y.
[13] H. Assadi, F. Gärtner, T. Stoltenhoff, H. Kreye, Bonding mechanism in cold gas spraying, Acta Mater. 51 (2003) 4379–4394, https://doi.org/10.1016/S1359-6454(03)00274-X.
[14] F.F. Raletz, M. Vardelle, G. Ezo'o, Critical particle velocity under cold spray conditions, Surf. Coat. Technol. 201 (2006) 1942–1947, https://doi.org/10.1016/j.surfcoat.2006.04.061.
[15] C.J. Li, W.Y. Li, H. Liao, Examination of the critical velocity for deposition of particles in cold spraying, J. Therm. Spray. Technol. 15 (2006) 212–222, https://doi.org/10.1361/105996306×108093.
[16] Q. Wang, N. Birbilis, M.X. Zhang, Process optimisation of cold spray Al coating on AZ91 alloy, Surf. Eng. 30 (2014) 323–328, https://doi.org/10.1179/1743294413Y.0000000224.
[17] X. Meng, J. Zhang, J. Zhao, Y. Liang, Y. Zhang, Influence of gas temperature on microstructure and properties of cold spray 304SS coating, J. Mater. Sci. Technol. 27 (2011) 809–815, https://doi.org/10.1016/S1005-0302(11)60147-3.
[18] P. Sudharshan Phani, D. Srinivasa Rao, S.V. Joshi, G. Sundararajan, Effect of process parameters and heat treatments on properties of cold sprayed copper coatings, J. Therm. Spray Technol. 16 (2007) 425–434, https://doi.org/10.1007/s11666-007-9048-1.
[19] R. Huang, H. Fukanuma, Study of the influence of particle velocity on adhesive strength of cold spray deposits, J. Therm. Spray Technol. 21 (2012) 541–549, https://doi.org/10.1007/s11666-011-9707-0.
[20] C. Chen, Y. Xie, X. Yan, S. Yin, H. Fukanuma, R. Huang, R. Zhao, J. Wang, Z. Ren, M. Liu, H. Liao, Effect of hot isostatic pressing (HIP) on microstructure and mechanical properties of Ti6Al4V alloy fabricated by cold spray additive manufacturing, Addit. Manuf. 27 (2019) 595–605, https://doi.org/10.1016/j.addma.2019.03.028.
[21] R. Jenkins, S. Yin, B. Aldwell, M. Meyer, R. Lupoi, New insights into the in-process densification mechanism of cold spray Al coatings: low deposition efficiency induced densification, J. Mater. Sci. Technol. 35 (2019) 427–431, https://doi.org/10.1016/j.jmst.2018.09.045.
[22] Y. Xie, S. Yin, J. Cizek, J. Cupera, E. Guo, R. Lupoi, Formation mechanism and microstructure characterization of nickel- aluminum intertwining interface in cold spray, Surf. Coat. Technol. 337 (2018) 447–452, https://doi.org/10.1016/j.surfcoat.2018.01.049.
[23] R. Huang, M. Sone, W. Ma, H. Fukanuma, The effects of heat treatment on the mechanical properties of cold-sprayed coatings, Surf. Coat. Technol. 261 (2015) 278–288, https://doi.org/10.1016/j.surfcoat.2014.11.017.
[24] P. Sudharshan Phani, V. Vishnukanthan, G. Sundararajan, Effect of heat treatment on properties of cold sprayed nanocrystalline copper alumina coatings, Acta Mater. 55 (2007) 4741–4751, https://doi.org/10.1016/j.actamat.2007.04.044.
[25] M. Yu, W.Y. Li, C. Zhang, H. Liao, Effect of vacuum heat treatment on tensile strength and fracture performance of cold-sprayed Cu-4Cr-2Nb coatings, Appl. Surf. Sci. 257 (2011) 5972–5976, https://doi.org/10.1016/j.apsusc.2011.01.076.
[26] X. Qiu, J. qiang Wang, N. ul H. Tariq, L. Gyansah, J. xuan Zhang, T. ying Xiong, Effect of heat treatment on microstructure and mechanical properties of A380 aluminum alloy deposited by cold spray, J. Therm. Spray Technol. 26 (2017) 1898–1907, https://doi.org/10.1007/s11666-017-0640-8.
[27] S. Yin, R. Jenkins, X. Yan, R. Lupoi, Microstructure and mechanical anisotropy of additively manufactured cold spray copper deposits, Mater. Sci. Eng. A 734 (2018) 67–76, https://doi.org/10.1016/j.msea.2018.07.096.
[28] S. Yin, Y. Xie, X. Suo, H. Liao, X. Wang, Interfacial bonding features of Ni coating on Al substrate with different surface pretreatments in cold spray, Mater. Lett. 138 (2015) 143–147, https://doi.org/10.1016/j.matlet.2014.10.016.
[29] Y. Zou, W. Qin, E. Irissou, J.G. Legoux, S. Yue, J.A. Szpunar, Dynamic recrystallization in the particle/particle interfacial region of cold-sprayed nickel coating: electron backscatter diffraction characterization, Scr. Mater. 61 (2009) 899–902, https://doi.org/10.1016/j.scriptamat.2009.07.020.
[30] Y. Zou, D. Goldbaum, J.A. Szpunar, S. Yue, Microstructure and nanohardness of cold-sprayed coatings: electron backscattered diffraction and nanoindentation studies, Scr. Mater. 62 (2010) 395–398, https://doi.org/10.1016/j.scriptamat.2009.11.034.
[31] M.R. Rokni, C.A. Widener, O.C. Ozdemir, G.A. Crawford, Microstructure and mechanical properties of cold sprayed 6061 Al in As-sprayed and heat treated condition, Surf. Coat. Technol. 309 (2017) 641–650, https://doi.org/10.1016/j.surfcoat.2016.12.035.
[32] X. Xie, C. Chen, Y. Ma, Y. Xie, H. Wu, G. Ji, E. Aubry, Z. Ren, H. Liao, Influence of annealing treatment on microstructure and magnetic properties of cold sprayed Ni-coated FeSiAl soft magnetic composite coating, Surf. Coat. Technol. 374 (2019) 476–484, https://doi.org/10.1016/j.surfcoat.2019.05.008.
[33] J.W. Murray, M.V. Zuccoli, T. Hussain, Heat treatment of cold-sprayed C355 Al for repair: microstructure and mechanical properties, J. Therm. Spray. Technol. 27 (2018) 159–168, https://doi.org/10.1007/s11666-017-0665-z.
[34] T. Schmidt, F. Gärtner, H. Assadi, H. Kreye, Development of a generalized parameter window for cold spray deposition, Acta Mater. 54 (2006) 729–742, https://doi.org/10.1016/j.actamat.2005.10.005.
[35] T. Schmidt, H. Assadi, F. Gärtner, H. Richter, T. Stoltenhoff, H. Kreye, T. Klassen, From particle acceleration to impact and bonding in cold spraying, J. Therm. Spray. Technol. 18 (2009) 794–808, https://doi.org/10.1007/s11666-009-9357-7.
[36] H. Yeom, T. Dabney, N. Pocquette, K. Ross, F.E. Pfefferkorn, K. Sridharan, Cold spray deposition of 304L stainless steel to mitigate chloride-induced stress corrosion cracking in canisters for used nuclear fuel storage, J. Nucl. Mater. 538 (2020), 152254, https://doi.org/10.1016/j.jnucmat.2020.152254.
[37] S. Yin, M. Meyer, W.Y. Li, H. Liao, R. Lupoi, Gas flow, particle acceleration, and heat transfer in cold spray: a review, J. Therm. Spray Technol. 25 (2016) 874–896, https://doi.org/10.1007/s11666-016-0406-8.
[38] Y. Xie, S. Yin, C. Chen, M.P. Planche, H. Liao, R. Lupoi, New insights into the coating/substrate interfacial bonding mechanism in cold spray, Scr. Mater. 125 (2016) 1–4, https://doi.org/10.1016/j.scriptamat.2016.07.024.
[39] C. Chen, Y. Xie, R. Huang, S. Deng, Z. Ren, H. Liao, On the role of oxide film's cleaning effect into the metallurgical bonding during cold spray, Mater. Lett. 210 (2018) 199–202, https://doi.org/10.1016/j.matlet.2017.09.024.
[40] V.K. Champagne, The cold spray materials deposition process, 2007. https://doi.org/10.1533/9781845693787.
[41] T. Schmidt, F. Gaertner, H. Kreye, New developments in cold spray based on higher gas and particle temperatures, Proc. Int. Therm. Spray Conf. (2006), https://doi.org/10.1361/105996306×147144.
[42] Y.K. Wei, X.T. Luo, Y. Ge, X. Chu, G.S. Huang, C.J. Li, Deposition of fully dense Al-based coatings via in-situ micro-forging assisted cold spray for excellent corrosion protection of AZ31B magnesium alloy, J. Alloys Compd. 806 (2019) 1116–1126, https://doi.org/10.1016/j.jallcom.2019.07.279.
[43] Y.K. Wei, X.T. Luo, X. Chu, G.S. Huang, C.J. Li, Solid-state additive manufacturing high performance aluminum alloy 6061 enabled by an in-situ micro-forging assisted cold spray, Mater. Sci. Eng. A 776 (2020), 139024, https://doi.org/10.1016/j.msea.2020.139024.
[44] Y.K. Wei, Y.J. Li, Y. Zhang, X.T. Luo, C.J. Li, Corrosion resistant nickel coating with strong adhesion on AZ31B magnesium alloy prepared by an in-situ shot-peening-assisted cold spray, Corros. Sci. 138 (2018) 105–115, https://doi.org/10.1016/j.corsci.2018.04.018.
[45] Y.K. Wei, X.T. Luo, C.X. Li, C.J. Li, Optimization of In-situ shot-peening-assisted cold spraying parameters for full corrosion protection of Mg alloy by fully dense Al-based alloy coating, J. Therm. Spray. Technol. 26 (2017) 173–183, https://doi.org/10.1007/s11666-016-0492-7.
[46] X.T. Luo, M.L. Yao, N. Ma, M. Takahashi, C.J. Li, Deposition behavior, microstructure and mechanical properties of an in-situ micro-forging assisted cold spray enabled additively manufactured Inconel 718 alloy, Mater. Des. 155 (2018) 384–395, https://doi.org/10.1016/j.matdes.2018.06.024.
[47] X.T. Luo, Y.K. Wei, Y. Wang, C.J. Li, Microstructure and mechanical property of Ti and Ti6Al4V prepared by an in-situ shot peening assisted cold spraying, Mater. Des. 85 (2015) 527–533, https://doi.org/10.1016/j.matdes.2015.07.015.

[48] X. Qiu, N. ul H. Tariq, L. Qi, J.Q. Wang, T.Y. Xiong, A hybrid approach to improve microstructure and mechanical properties of cold spray additively manufactured A380 aluminum composites, Mater. Sci. Eng. A 772 (2020), 138828, https://doi.org/10.1016/j.msea.2019.138828.

[49] D. Rui, X. Li, W. Jia, W. Li, W. Xiao, T. Gui, Releasing kinetics of dissolved copper and antifouling mechanism of cold sprayed copper composite coatings for submarine screen doors of ships, J. Alloys Compd. 763 (2018) 525–537, https://doi.org/10.1016/j.jallcom.2018.05.355.

[50] Aaron T. Nardi, Tahany Ibrahim El-Wardany, William Werkheiser, Michael A. Klecka, Method for enhancing bond strength through in-situ peening, US9938624B2, 2018.

[51] Y. Xie, C. Chen, M.P. Planche, S. Deng, R. Huang, Z. Ren, H. Liao, Strengthened peening effect on metallurgical bonding formation in cold spray additive manufacturing, J. Therm. Spray. Technol. 28 (2019) 769–779, https://doi.org/10.1007/s11666-019-00854-4.

[52] A.T.N. Michael, A. Klecka, Self-peening feedstock materialsfor cold spray deposition, US9890460B2, 2018.